

On the spatial distribution of electron energy loss due to gyro-cooling in hot-star magnetospheres

B. Das^{1,2*} and S. P. Owocki¹

¹*Department of Physics and Astronomy, University of Delaware, 217 Sharp Lab, Newark, Delaware, 19716, USA*

²*CSIRO Space and Astronomy, PO Box 1130, Bentley WA 6102, Australia*

ABSTRACT

Hot magnetic stars often exhibit incoherent circularly polarized radio emission thought to arise from gyro-synchrotron emission by energetic electrons trapped in the circumstellar magnetosphere. Theoretical scalings for electron acceleration by magnetic reconnection driven by centrifugal breakout match well the empirical scalings for observed radio luminosity with both the magnetic field strength and the stellar rotation rate. This paper now examines how energetic electrons introduced near the top of closed magnetic loops are subsequently cooled by the energy loss associated with their gyro-synchrotron radio emission. For sample assumed distributions for energetic electron deposition about the loop apex, we derive the spatial distribution of the radiated energy from such “gyro-cooling”. For sub-relativistic electrons, we show explicitly that this is independent of the input energy, but also find that even extensions to the relativistic regime still yield a quite similar spatial distribution. However, cooling by coulomb collisions with even a modest ambient density of thermal electrons can effectively quench the emission from sub-relativistic electrons, indicating that the observed radio emission likely stems from relativistic electrons that are less affected by such collisional cooling. The overall results form an initial basis for computing radio emission spectra in future models that account for such cooling and multimode excitation about the fundamental gyro-frequency. Though motivated in the context of hot-stars, the basic results here could also be applied to gyro-emission in any dipole magnetospheres, including those of ultra-cool dwarfs and even (exo)-planets.

Key words: stars: magnetic fields – stars: early type – stars: rotation – radio continuum: stars – magnetic reconnection

1 INTRODUCTION

Hot magnetic stars with moderately rapid rotation show incoherent, circularly polarized radio emission, thought to arise from gyro-synchrotron emission of energetic electrons trapped in magnetic loops (e.g. Drake et al. 1987; Andre et al. 1988; Trigilio et al. 2004). Empirical analyses show that the radio emission depends on both the magnetic field strength and the stellar rotation rate (Leto et al. 2021; Shultz et al. 2022), with a scaling that is well explained by a model in which the electrons are energized by magnetic reconnection events that arise from centrifugal breakout (CBO) of plasma trapped in the rotating magnetosphere (Owocki et al. 2022). Building thus on a scenario in which energetic electrons are introduced around the apex of closed magnetic loops, the present paper examines how the energy lost to gyro-synchrotron radio emission cools the electrons,

and how this affects the spatial and spectral distribution of the observed radio emission.

In the subset ($\sim 10\%$; Grunhut et al. (2017); Sikora et al. (2019)) of OBA stars with strong (> 100 G; Aurière et al. (2007); Shultz et al. (2019)), globally ordered (often significantly dipolar; Kochukhov et al. (2019)) magnetic fields, the trapping of stellar wind outflow by closed magnetic loops leads to the formation of a circumstellar *magnetosphere* (Petit et al. 2013). Because of the angular momentum loss associated with their relatively strong, magnetised wind (ud-Doula et al. 2009), magnetic O-type stars are typically slow rotators, with trapped wind material falling back on a dynamical timescale, giving what’s known as a “dynamical magnetosphere” (DM).

But in cooler magnetic stars (spectral type B or even A), the relatively weak stellar winds imply longer spin-down times, and so a significant fraction that still retain a moderately rapid rotation. For cases in which the associated Keplerian co-rotation radius R_K lies within the Alfvén radius R_A

* E-mail: Barnali.Das@csiro.au

that characterises the maximum height of closed loops, the rotational support leads to formation of a “*centrifugal magnetosphere*” (CM). Recent work has shown how the *centrifugal breakout* (CBO) from such CM’s plays a key role in both their Balmer line emission (Shultz et al. 2020; Owocki et al. 2020), as well as their incoherent radio emission (Owocki et al. 2022).

As a basis toward developing predictive models of such radio emission, the analysis here assumes that repeated CBO-driven magnetic reconnection events seed a quasi-steady, gyrotropic population of energetic electrons around the tops of underlying closed magnetic loops. As in the standard scenario (e.g. Leto et al. 2021), the spiraling of these energetic electrons as they mirror between the opposite foot-points of the loop leads to the gyro-synchrotron emission of the observed radio.

In the past, Triglio et al. (2004) presented a three-dimensional numerical model to calculate gyro-synchrotron radio emission from hot magnetic stars using a set of free parameters related to the stellar magnetospheres. This model is based on the scenario proposed by Andre et al. (1988), wherein electrons are accelerated to relativistic energies at a current sheet that lies at the magnetic equator near the Alfvén radius; these electrons travel towards the star following the magnetic field lines and emit non-thermal radio emission. It is assumed that the non-thermal electrons have a power-law distribution in energy, but maintains an isotropic distribution at all points of the ‘middle magnetosphere’ (e.g. Triglio et al. 2004). This model has been used in several subsequent works (e.g. Leto et al. 2006, 2012, 2021, etc.) to estimate different stellar parameters via comparison with observed radio emission.

In the present study, we investigate how the energy emitted by the non-thermal electrons depends on the details of the energy ‘deposition’ in the magnetosphere. While doing this, we self-consistently consider the time-evolution of the electron pitch-angles due to loss of energy via radiation (i.e. the effect of non-conservation of magnetic moment). Our work is motivated from recent empirical results that the current sheet near the Alfvén radius cannot be the main source of non-thermal electron production in stars with centrifugal magnetospheres (Leto et al. 2021; Shultz et al. 2022); instead CBO events are more favoured candidates to explain the observed relation of radio luminosity with stellar rotation and other parameters (Shultz et al. 2022; Owocki et al. 2022). Our ultimate goal is to understand the physical process(es) that produce(s) the non-thermal electrons in hot-star magnetospheres. This work is the first step towards that goal of connecting the observed properties of radio emission with that of the phenomenon responsible for generating the relativistic electrons.

As detailed in the next section (§2.1), for magnetic field strengths $\gtrsim 100$ G that are associated with B-star CM’s, the electron cooling time due to radiation of energy is less than a day, and so comparable to or shorter than the characteristic timescales for wind outflow and filling the CM¹. After

reviewing the general features of propagation and mirroring of electrons along a closed loop (§2.2), we derive (§3.1) the basic coupled differential equations for loss rate of electron energy, and the associated evolution of its magnetic moment. For the common case that the electron propagation time is much smaller than its cooling time, solutions show (§3.2) that the spatial distribution of radio emission along the loop follows a distinctive form (Figure 5), with a narrow peak near the loop apex, and broader wings extending down to sharp cutoffs due to truncation from the underlying star. We then explore models with energy deposition that have gaussian distributions in radius and latitude (§4.1), deriving the associated spatial distribution of energy lost due to gyrocooling (§4.2). Following a brief analysis (§4.3) of the cooling effect of coulomb collisions with thermal electrons, we conclude (§5) with a brief summary and outline for future work. The appendix presents generalized equation forms for relativistic electrons.

2 BACKGROUND

2.1 Gyro-synchrotron cooling

For a potentially relativistic electron with pitch-angle α in gyration about a local magnetic field, the associated synchrotron power emitted is given by Condon & Ransom (2016, their eq. (5.37)),

$$P = 2\sigma_T\beta^2\gamma^2cU_B \sin^2\alpha, \quad (1)$$

where $U_B \equiv B^2/8\pi$ is the (cgs) energy density of the magnetic field B ; $\sigma_T = 0.67 \times 10^{-24}$ cm² is the Thomson cross section for electron scattering; $\beta \equiv v/c$ is the ratio of electron speed v to the speed of light c ; and $\gamma \equiv 1/\sqrt{1-\beta^2}$ is the associated relativistic energy factor.

For electron mass m_e , the associated electron kinetic energy is $\text{KE} = (\gamma - 1)m_e c^2$. Averaging the power loss over a given pitch-angle distribution $\langle P \rangle \sim \langle \sin^2\alpha \rangle$, we can then define an electron energy-loss time as $t_e \equiv \text{KE}/\langle P \rangle$, which, after some manipulation, can be shown to scale as

$$\begin{aligned} t_e &= \frac{4\pi m_e c}{\sigma_T (1 + \gamma) B^2 \langle \sin^2\alpha \rangle} \\ &= \frac{5.16 \times 10^8 \text{ s}}{(1 + \gamma) \langle \sin^2\alpha \rangle} \left(\frac{1 \text{ G}}{B} \right)^2. \end{aligned} \quad (2)$$

For non-relativistic electrons (i.e. with $\gamma \gtrsim 1$) with a given pitch angle distribution, note that this cooling time depends *only* on the magnetic field strength, and not, e.g., on the electron speed or energy.

For the simple case of a gyrotropic distribution (for which $\langle \sin^2\alpha \rangle = 2/3$) and a canonical field $B = 1$ G, the latter relation in (2) shows that the loss time is more than a decade (recalling that $1 \text{ yr} \approx 3 \times 10^7 \text{ s}$).

However, in the context of massive-star magnetospheres, this loss timescale can be much shorter. Analyses by Shultz et al. (2022) and Owocki et al. (2020) have shown that H-alpha emission requires a field at the Kepler radius $B_K \approx 100$ G, implying a cooling time for non-relativistic

¹ Within the general lack of strong variability in the observed incoherent radio flux (e.g. Triglio et al. 2000; Das & Chandra 2021, etc.), this supports the evidence from similarly steady H α and continuum flux observations (Shultz et al. 2020; Owocki et al.

2020) that CBO occurs not in sporadic, large-scale events, but rather through a quasi-steady stream of smaller outbursts.

electrons, $t_e \approx 5.1 \times 10^4 \text{ s} \approx 0.6 \text{ d}$. The implication is then that the observed quasi-steady circularly polarized gyro-synchrotron radio emission must be replenished by many small centrifugal breakouts that occur on such a timescale of order a day or less.

On the other hand, this loss time is generally much *longer* than the typical propagation time of such energetic electrons across loops. As an example, for 25 keV electrons with speed $v \approx c/3$, the characteristic advection time across of loop of apex radius r_a is

$$t_a \equiv \frac{r_a}{v} \approx 100 \text{ s} \frac{r_a}{10^{12} \text{ cm}}. \quad (3)$$

Comparison with eqn. (2) shows that for a loop with $r_a \approx 10^{12} \text{ cm}$ and $B_a \approx 100 \text{ G}$, $t_a \ll t_e$. As detailed below, this implies that electrons will generally mirror many times across a dipole loop as they gradually lose energy.

2.2 Magnetic mirroring

An electron with energy E and pitch angle α gyrating around field of local strength B has a magnetic moment given by

$$p_m \equiv E \sin^2 \alpha / B. \quad (4)$$

Under the common assumption of fixed energy E , this magnetic moment is also conserved. For electrons with pitch angle α_a at the apex radius r_a of a loop with apex field strength B_a , the pitch angle will thus become perpendicular ($\sin \alpha = 1$) at a mirror radius r_m , with field strength

$$B_m = \frac{B_a}{\sin^2 \alpha_a}. \quad (5)$$

For a simple dipole field with spatial scaling $B \sim \sqrt{1 + 3\mu^2}/r^3$ in radius r and colatitude cosine $\mu = \sqrt{1 - r/r_a}$, this leads to a sixth-order polynomial for r_m ,

$$\left(\frac{r_m}{r_a}\right)^6 = \sin^4 \alpha_a (4 - 3r_m/r_a). \quad (6)$$

The simple approximation $r_m/r_a \approx \sin^{2/3} \alpha_a$ is within a few percent of the full solution except for the small pitch angle regime. For the analysis presented in the subsequent sections, we have used the full solution.

3 COOLING ALONG LOOP

3.1 Dimensionless ODE for energy loss

More generally, the time variation of energy dE/dt associated with the gyro-synchrotron radiation leads to an associated change in the magnetic moment,

$$\frac{dp_m}{dt} = \frac{1}{B} \frac{dE}{dt}. \quad (7)$$

For an electron with speed v , energy $E = m_e v^2/2$, and pitch angle α , the gyro-emission power P from eqn. (1) gives for the time change of energy,

$$\frac{dE}{dt} = -P \approx -\frac{\sigma_T}{2\pi m_e c} E B^2 \sin^2 \alpha = -\frac{\sigma_T}{2\pi m_e c} p_m B^3, \quad (8)$$

where the second equality applies for the non-relativistic case $\gamma \approx 1$, and the final equality uses the definition of

magnetic moment $p_m = E \sin^2 \alpha / B$ to eliminate α in favor of B/E .

The initial analysis here focuses on this sub-relativistic case because then the relative cooling becomes independent of the electron energy, depending only on the magnetic field strength B and electron pitch angle α . Appendix A derives the generalized equations for relativistic electrons.

Defining apex-scaled variables for energy $e \equiv E/E_a$ and magnetic field $b \equiv B/B_a$, along with scaled magnetic moment $p \equiv p_m B_a/E_a$, eqns. (8) and (7) can be recast as a coupled system of two first-order, dimensionless ODE's,

$$\frac{de}{dt} = -k p b^3, \quad (9)$$

and

$$\frac{dp}{dt} = \frac{1}{b} \frac{de}{dt}, \quad (10)$$

where the dimensionless constant k is given by

$$k \equiv \left[\frac{\sigma_T B_a^2}{2\pi m_e c} \right] \frac{r_a}{v_a} \equiv \frac{t_a}{t_c}. \quad (11)$$

In the latter equality, $t_a \equiv r_a/v_a$ is a characteristic propagation time, used now to scale the time variable, $t \rightarrow t/t_a$. The cooling constant k is thereby cast as the ratio of this to a characteristic cooling time t_c , given by the inverse of the square bracket term².

For typical values $r_a = 10^{12} \text{ cm}$, $B_a = 100 \text{ G}$, $E_a = 25 \text{ keV}$, and $v_a = c/3$, we find this cooling constant is quite small, $k \approx 0.002$. For initial pitch angles that are not too small, with thus mirroring not too far below the loop apex, only a small fraction of the particles energy is lost per mirror cycle. But the cubic scaling of cooling with magnetic field, and its steep increase inward, means that lower pitch angles can lose a significant fraction of their energy near their mirror point.

The apex-scaled dipole field b can be written as a function of the co-latitude cosine μ ,

$$b(\mu) \equiv \frac{B(\mu)}{B_a} = \frac{\sqrt{1 + 3\mu^2}}{(1 - \mu^2)^3}. \quad (12)$$

A key to proceeding thus regards the time variation of this co-latitude variable, $d\mu/dt$. For electron speed v , movement along the field line coordinate s is given by

$$v \cos \alpha = \frac{ds}{dt} = \frac{r(d\theta/dt)}{b_\theta} = r_a \sqrt{1 + 3\mu^2} \frac{d\mu}{dt}, \quad (13)$$

where $b_\theta = \sqrt{1 - \mu^2}/\sqrt{1 + 3\mu^2}$ is latitudinal projection of the unit vector along the dipole field, for which also $r = r_a(1 - \mu^2)$. Using eqn. (11) and the above definitions of scaled energy e and scaled magnetic moment p , we can write a third dimensionless time equation that must be solved,

$$\frac{d\mu}{dt} = -\text{Sign}(\cos \alpha) \frac{\sqrt{e - p b}}{\sqrt{1 + 3\mu^2}}, \quad (14)$$

where the sign function allows one to keep track the directionality of propagation as the electron mirrors across the loop.

² This is closely related to the electron energy loss time for a specific pitch angle, as given by eq. (2).

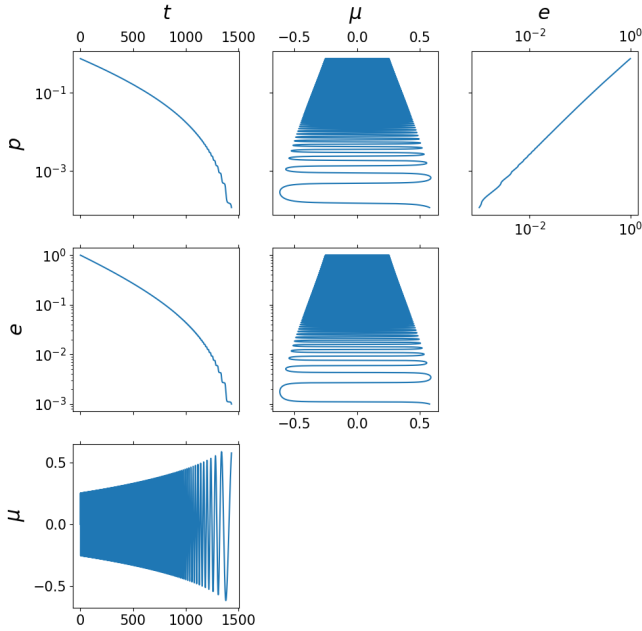


Figure 1. Solutions to the set of equations described in §3.1. The independent variable is the dimensionless time t . The particle starts at the loop apex ($\mu = 0$) with an initial pitch angle of 60° . For the definitions of t , μ , e and p , refer to §3.1.

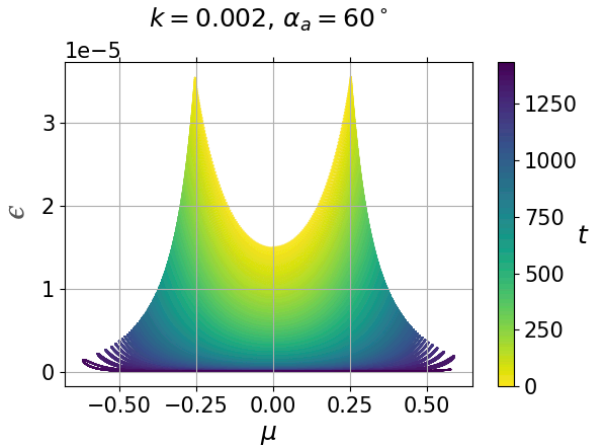


Figure 2. Color-coded time variation of energy emission ϵ plotted vs. co-latitude μ , for the standard case with apex pitch angle $\alpha_a = 60^\circ$ and cooling parameter $k = 0.002$.

In this approach, one solves the coupled system of 3 ODE's (14), (9), and (10) for the associated dependent variables μ , e , and p as a function of the independent variable, the scaled time t . Appendix A gives the corresponding relativistic forms, (A3), (A5) and (A6), wherein the curly bracket factors represent the corrections from the sub-relativistic expressions here.

3.2 Energy deposition at loop apex

In our basic scenario here, we assume electrons are introduced at a dipole loop apex with fixed energy and pitch angle α_a , giving then initial conditions $\mu(0) = 0$, $e(0) = 1$,

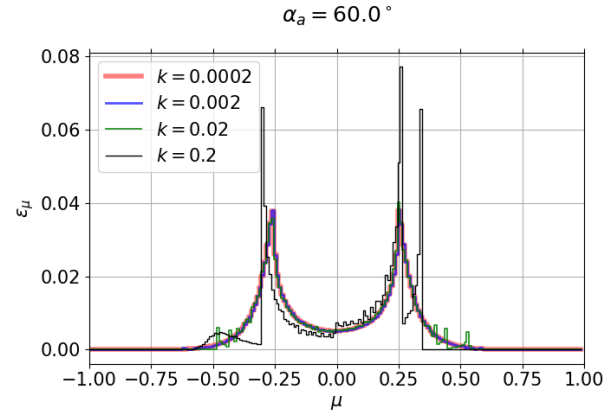


Figure 3. For the sample initial pitch angle case $\alpha_a = 60^\circ$, the distribution of total energy emission ϵ_μ in co-latitude μ , for the four labeled values of the cooling parameter k .

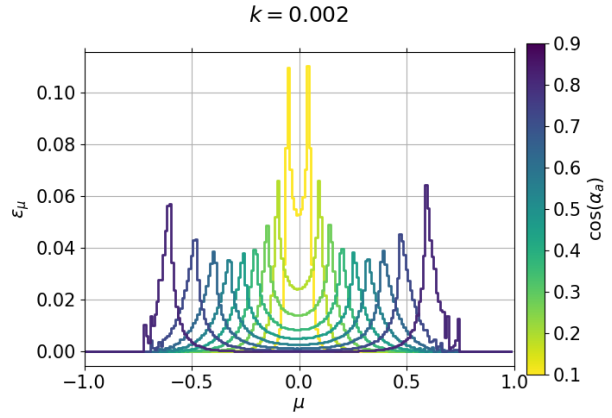


Figure 4. Total energy emission ϵ_μ versus co-latitude μ for the labeled range of $\cos \alpha_a$.

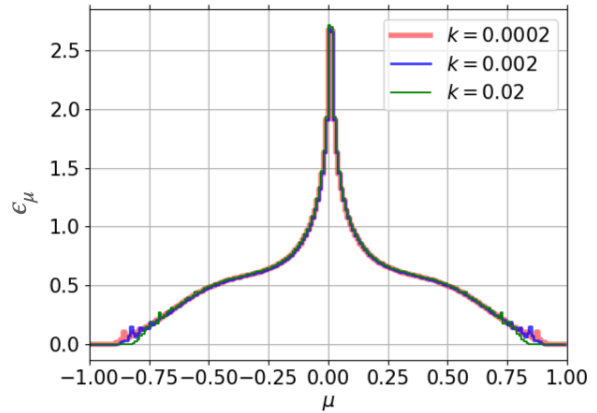


Figure 5. The cumulative energy emission for an initially gyrotropic pitch angle distribution, overplotting ϵ_μ versus co-latitude μ for three small values of the cooling constant. The curves are normalized such that the total energy lost, as reflected by the area under the curves, is unity.

and $p(0) = \sin^2 \alpha_a$. From this initial condition, we use the odeint function from `scipy.integrate` (Virtanen et al. 2020) to evolve the system of ODE's (9), (10), and (14) in time until the energy retained by the electron drops below 0.1% of its initial energy.

Figure 1 shows solutions for a representative case with $k = 0.002$ and $\alpha_a = 60^\circ$. The upper two panels of the left column plot the temporal decrease in the magnetic moment and energy, while the bottom panel shows the temporal variation of the co-latitude (due to magnetic mirroring). Note how the non-conservation of magnetic moment leads to a systematic increase in the mirror co-latitude, from its initial $|\mu_{min}| \approx 0.24$ to a maximum $\mu_{max} \approx 0.55$, corresponding to a minimum radius $r_{min}/r_a \approx 1 - \mu_{max}^2 \approx 0.7$. For any loop with apex $r_a/R_* > 1/0.7 \approx 1.4$, electrons with this initial pitch angle $\alpha_a = 60^\circ$ will thus have their full energy dissipated without interaction with the underlying star. We thus defer consideration of such stellar interaction dissipation to the fuller models below.

The central column of Figure 1 shows the associated evolution of magnetic moment and energy with co-latitude. The latter in particular forms the basis for deriving the spatial distribution of energy loss along the loop. Figure 2 plots the energy emission ϵ versus co-latitude μ , color coded by the deposition time.

By binning the energy loss over a grid in co-latitude, Figure 3 plots the total *distribution* of emission ϵ_μ in co-latitude μ , comparing now results for the various labeled values of the cooling parameter k . Note that results for the smallest k are all very similar, since they all represent the cumulative effects of energy loss over many mirror cycles; in contrast, for the case with cooling constant $k = 0.2$ approaching unity, the relatively stronger energy loss within any given mirror cycle gives a much more irregular distribution.

For the standard cooling parameter $k = 0.002$, Figure 4 overplots the energy emission ϵ_μ versus co-latitude μ for a range of initial pitch angles ranging from $\cos(\alpha_a) = 0.1$ to 0.9. The peak energy emission again occurs near the mirror point for each initial pitch angle, with a narrow spread. But these mirror points range from near the loop apex for oblique pitch angles (e.g., $\cos \alpha_a = 0.1$) to much further down the loop for more field-aligned cases (e.g., $\cos \alpha_a = 0.9$).

Figure 5 plots the total energy emission for a *gyrotropic* distribution of initial pitch angles, assuming the labeled small values for the cooling parameter k . The close overlap for all 3 cases shows that this spatial distribution of energy is not sensitive to the exact cooling parameter, as long as it is significantly below unity, and so allows for gradual cumulative energy loss over many mirror cycles.

The strong peak around $\mu = 0$ reflects the strong energy emission near the loop apex from electrons with nearly orthogonal initial pitch angles $\alpha_a \approx 90^\circ$, which, due to the relatively large solid angle, are relatively more numerous. But more field-aligned pitch-angles contribute to significant energy emission further down the loop, here extending to a maximum colatitude $|\mu_{max}|$ that depends on just how small the cooling parameter k is.

4 MODELS WITH EXTENDED SPATIAL DEPOSITION OF ENERGETIC ELECTRONS

Building upon this analysis of the idealized case that energetic electrons are introduced at the apex of a single dipole loop, let us next generalize this to more realistic models in which the electron source is distributed over a range of loop heights and positions around the loop apex.

4.1 Gaussian deposition in co-latitude

We first consider the case in which the initial energy deposition along a given loop follows a gaussian form that is still centered on the loop apex $\mu = 0$, but with co-latitude dispersion σ_μ ,

$$e_\mu = C_\mu \exp\left(-\frac{\mu^2}{2\sigma_\mu^2}\right), \quad (15)$$

where for a loop with apex radius r_a , C_μ is a normalization constant that ensures that the total energy ($\int e_\mu d\mu$) is unity ($e = 1$) when integrated from the loop apex ($\mu = 0$) to the stellar base ($\mu = \pm\mu_* \equiv \pm\sqrt{1 - (R_*/r_a)}$).

For a loop with $r_a = 3R_*$, the top panel of Figure 6 compares the associated cumulative energy emission ϵ_μ vs. co-latitude μ for cases with $\sigma_\mu = 0.1, 0.3,$ and 0.5 . For the small dispersion case $\sigma_\mu = 0.1$, the cumulative energy loss still has its peak at the loop apex, though with a broader range than found for models with energy deposition confined to just the loop apex.

For intermediate dispersion case $\sigma_\mu = 0.3$, the central emission is flatter, with even a modest dip around $\mu = 0$.

Indeed, for the largest dispersion case $\sigma_\mu = 0.5$, the central emission shows an even deeper local minimum, even though that is still where the deposition is greatest. Instead there are two distinct peaks located at $|\mu| \approx 0.5$, distinctly below the loop apex, where the energy deposition is highest.

To help understand this rather unexpected result, the light green curves in the bottom panel plot the emission distribution for a subset with deposition peaks separated by $\Delta\mu = 0.1$, showing then these generally have much stronger emission away from the apex, due the higher magnetic field strength there. Thus, even though the black dots show these represent a somewhat lower number in the gaussian distribution, their higher emission leads to an overall peak in the cumulative emission at co-latitudes $|\mu| \approx 0.5 = \sigma_\mu$.

These results have important implications for both the spatial and spectral distribution of radio emission for more realistic models in which the energy deposition has a broader radial distribution, as we discuss next.

4.2 Emission intensity from Gaussian deposition in radius and co-latitude

Let us now consider a model in which the initial energy deposition has a gaussian spread in both field co-latitude $\mu = \sqrt{1 - r/r_a}$ and apex radius $r_a = r/(1 - \mu^2)$, centered on a peak radius r_p with radial dispersion σ_r ,

$$e_{\mu,r_a} = C_a \exp\left[-\frac{(r_a - r_p)^2}{2\sigma_r^2}\right] e_\mu, \quad (16)$$

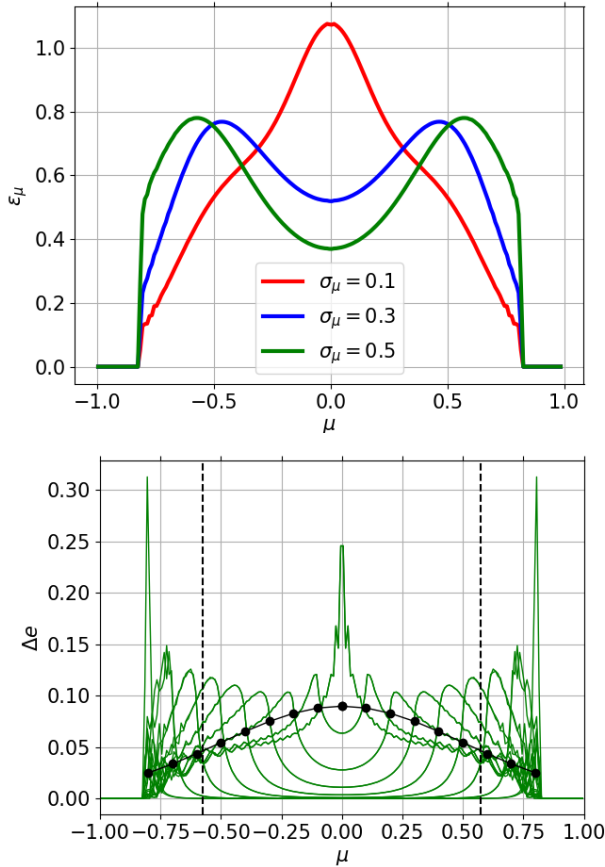


Figure 6. Top: For a sample loop with apex at $r_a = 3R_*$, the energy loss ϵ_μ versus co-latitude μ for latitudinal dispersions $\sigma_\mu = 0.1, 0.3$, and 0.5 . In all cases, the total energy deposited $e = 1$, but due to losses to the underlying star (as indicated by the sharp cutoffs at large $|\mu|$), the total emission is slightly less than unity, viz. $\langle \Delta e \rangle = 0.986, 0.985$, and 0.956 for $\sigma_\mu = 0.1, 0.3$, and 0.5 , respectively. Bottom: For the large dispersion case $\sigma_\mu = 0.5$, the green curves break down the emission from a subset of energy distributions with peaks shown by the bold black dots. The sum of this subset forms the double peaks at location marked here by the vertical dashed lines. The area under each curve represents the total energy emitted corresponding to the energy deposition at a given μ .

where C_a is a normalization factor such that

$$\int_{R_*}^{\infty} \int_{-\mu_*}^{+\mu_*} e_{\mu, r_a} d\mu dr_a = 1,$$

where $\mu_* \equiv \sqrt{1 - R_*/r_a}$.

Given such a distribution in energy deposition e_{μ, r_a} , one can, for each r_a , use the techniques described above to derive an associated emission distribution ϵ_{μ, r_a} along the loop. For differential intervals in loop colatitude $d\mu$ and apex radius dr_a , the incremental contribution to radio *luminosity* is given by

$$dL = \epsilon_{\mu, r_a} d\mu dr_a. \quad (17)$$

Assuming for simplicity that the local emission is isotropic over the full 4π steradians, the associated increment in *intensity* (energy/time/area/solid angle) about an azimuthal

interval $d\phi$ centered on the plane of the sky is

$$\frac{dI}{d\phi} = \frac{dL}{4\pi r d\theta dr} = \frac{\epsilon_{\mu, r_a}}{4\pi r \sqrt{1 - \mu^2}}, \quad (18)$$

where the latter equality uses the relations $d\mu = \sqrt{1 - \mu^2} d\theta$ and $dr_a = dr/(1 - \mu^2)$.

For a representative, standard case with $r_p = 3R_*$ and $\sigma_r = 0.5R_*$, the lower row of Figure 7 shows the spatial variation of this emitted intensity $dI/d\phi$ for the 3 distinct values of latitudinal dispersion $\sigma_\mu = 0.1, 0.3$, and 0.5 . The white lines show contours of the field strength B , spaced logarithmically in increments of -0.1 dex from the value at the equatorial surface.

The upper row of Figure 7 compares the corresponding emission for a simple “on-the-spot” model, in which the local emission is just set by the local energy deposition, $\epsilon_{\mu, r_a} = e_{\mu, r_a}$. Comparison with the middle row shows that the net effect of the electron propagation and mirroring within the closed loops is to shift the emission closer to loop footpoints, where the field strength is higher. This shift becomes more pronounced with increasing latitudinal dispersion σ_μ .

Using the generalized relativistic forms for gyro-cooling derived in Appendix A, the lower row shows a similar spatial distribution for the relativistic case with initial Lorentz factor $\gamma_a = 11$ at the loop apex. The close similarity to the middle panel shows that the relativistic corrections have only a modest effect on the overall spatial distribution of gyro-cooling emission.

The results derived in this subsection (including Figure 7) provides a visualization about the relation between the spatial distribution of energy deposited and that of the energy radiated by the non-thermal electrons. In their current forms, however, these results cannot be compared with observations, which will require a more complete treatment, including absorption effects in the magnetosphere.

4.3 Cooling by collisions with thermal electrons

In addition to the gyro-cooling examined here, non-thermal electrons can also cool by the energy exchange from coulomb collision with an ambient population of thermal electrons of much lower energy (see Güdel 2009, e.g., their section 8.4.3). For potentially relativistic electrons with Lorentz factor γ and thus kinetic energy $E = (\gamma - 1)m_e c^2$, the coulomb collision cross section takes the form

$$\sigma_c = \frac{4\pi e^4}{m_e^2 c^4} \frac{\ln \Lambda}{(\gamma - 1)^2} = \frac{3}{2} \frac{\ln \Lambda \sigma_T}{(\gamma - 1)^2} \approx \frac{2 \times 10^{-23} \text{cm}^2}{(\gamma - 1)^2}, \quad (19)$$

where the last evaluation assumes a characteristic value $\ln \Lambda \approx 20$ for the coulomb logarithm (which accounts for the cumulative effect of many small-angle scatterings). Since each associated collision results in the effective loss of the kinetic energy of the non-thermal particle, the associated cooling time for collisions with thermal electrons of number density n_e is (Leach & Petrosian 1981, see their eqn. 1)

$$t_c = \frac{\beta}{n_e \sigma_c c (\gamma - 1)} = 1.7 \times 10^{12} \text{s} \frac{\beta (\gamma - 1)}{n_e}. \quad (20)$$

Comparison with eqn. (2) shows that the ratio of coulomb to gyro-synchrotron cooling (assuming an isotropic pitch-angle distribution with $\langle \sin^2 \alpha \rangle = 2/3$) is given by

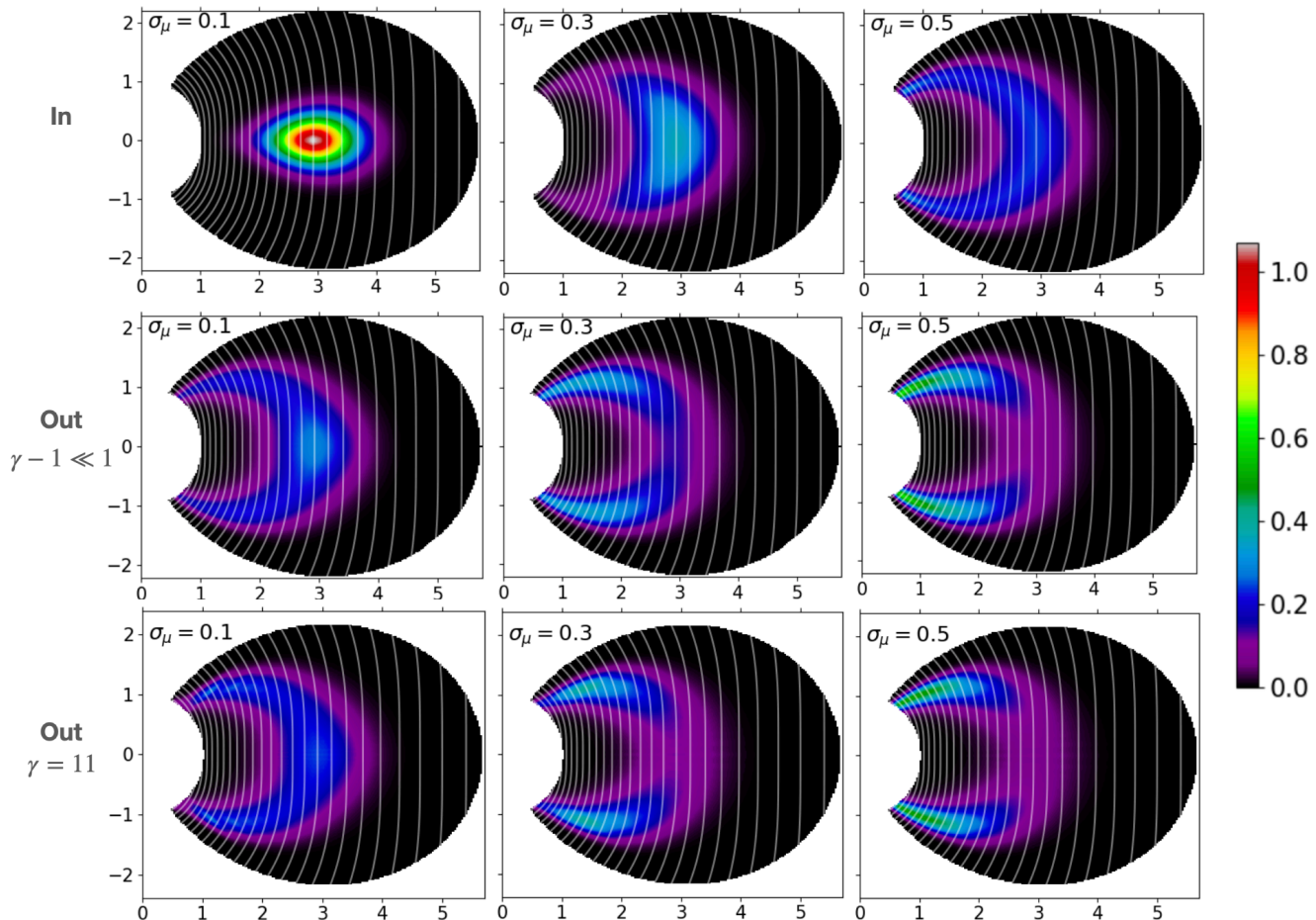


Figure 7. Middle row: Spatial variation of emission intensity increment $dI/d\phi$ (eqn. 18) from a small azimuthal wedge centered on the plane of the sky, for the gaussian energy deposition model (eqn. 16), assuming $r_p = 3R_*$, $\sigma_r = 0.5R_*$, and the 3 labeled values of $\sigma_\mu = 0.1, 0.3,$ and 0.5 . Top row: Associated intensity for a simpler “on-the-spot” model, with local emission set to local energy deposition, $\epsilon_{\mu,r_a} = \epsilon_{\mu,r_a}$. Bottom row: Same as middle row but for case of relativistic electrons with initial $\gamma = 11$. Comparison of the top vs. middle/bottom rows thus illustrates the differences in energy deposition *input* vs. emission *output* for both relativistic and non-relativistic electrons. In all panels, the total integrated emission is normalized to unity. The white lines represent contours of magnetic field strength B , spaced logarithmically by -0.1 dex from the stellar surface value at the magnetic equator. Note that, while these figures do not directly connect to observed radio intensity, they do illustrate how the spatial distribution of energy deposition in the magnetosphere influences the spatial (and also spectral) distribution of resulting radiation by the non-thermal electrons.

$$\frac{t_c}{t_e} \approx 2.2 \times 10^9 \frac{(\gamma^2 - 1)\beta B_{kG}^2}{n_e}, \quad (21)$$

where $B_{kG} \equiv B/kG$ and n_e is in cm^{-3} . Setting the left side to unity, we can solve for the critical density above which cooling by coulomb collisions will dominate over gyro emission,

$$n_{e1} \approx 2.2 \times 10^9 (\gamma^2 - 1)\beta B_{kG}^2. \quad (22)$$

For highly relativistic electrons with $\gamma \gg 1$ and $\beta \rightarrow 1$, this critical density increases with γ^2 , implying that in regions with strong kG fields, coulomb cooling will only be important in regions with quite a high density of thermal electrons.

In contrast, for non-relativistic electrons with $\beta < 1$, we find $n_{e1} \sim \beta^3$, implying that cooling by coulomb collisions will dominate over gyro-emission for even modest densities.

For example, for the mildly sub-relativistic case $\beta = 1/3$, we find $n_{e1} = 7.2 \times 10^7 \text{ cm}^{-3} B_{kG}^2$.

The overall implication is that the incoherent radio emission from magnetic hot stars most likely arises from relativistic electrons for which gyro-emission is relatively unaffected by collisional losses with thermal electrons. Further quantifying this will depend on the detailed models of the thermal electron density and its spatial distribution. We are currently examining such cooling effects in the context of hot-stars with centrifugal magnetospheres, and will report results in a follow up paper.

5 SUMMARY AND FUTURE WORK

5.1 Result summary

The incoherent, circularly polarized radio emission observed from magnetic massive stars is understood to arise from

gyro-synchrotron emission by energetic electrons trapped within their magnetospheres. By accounting for the associated “gyro-cooling” loss of energy, this paper analyzes the spatial distribution of this radio emission for a simple model in which the electrons trapped within closed (assumed dipole) magnetic loops gradually cool as they repeatedly mirror across the loop. Some key results are:

- Because the gyro-cooling time in hot-star magnetospheres is of order a day, explaining their observed persistent quasi-steady radio emission requires a persistent electron acceleration mechanism, perhaps from magnetic reconnection driven by repeated, small-scale centrifugal breakout (CBO) events in these rapidly rotating magnetospheres (Owocki et al. 2022).

- So long as the ratio of the advective propagation time to cooling time is small, $k \equiv t_a/t_c \ll 1$, the spatial distribution of cumulative emission is insensitive to the specific value of this ratio.

- For various assumptions for the spatial location of the deposition of energetic electrons centered about the apex of closed magnetic loops, the associated radio emission tends to be spread down the loop where the field is stronger (see Figure 7). The formalism here thus effectively represents an energy transport model between the deposition of energetic electrons to their ultimate gyro-synchrotron radio emission.

- Generalization to the case of relativistic electrons introduces a formal, explicit dependence of gyro-cooling on the initial energy, but the overall effect on the resulting spatial distribution of emission is quite modest.

- Cooling from coulomb collisions with thermal electrons in the dense CM layer should effectively quench any gyro-emission from sub-relativistic electrons, but have less effect on relativistic electrons.

5.2 Future extensions

While the work here thus provides an initial basis for modelling the spatial and spectral distribution of radio emission from these massive-star magnetospheres, it is grounded in several idealized assumptions and simplifications that should be examined and relaxed in future work.

- To translate results for spatial distribution of emission within magnetic loops into observable spectra in frequency, future work should consider a realistic scenario of multiple harmonic emission and absorption in the stellar magnetosphere.

- This should include the effect of cooling of the energetic electrons through coulomb collision with thermal electrons associated with material trapped within the centrifugal magnetosphere.

- In contrast to the static, dipole field assumed here, even closed loops in centrifugal magnetospheres are likely to be dynamically distorted, due to the stretching by the centrifugal force from the trapped material and the associated breakout events. Future work should examine how this affects electron mirroring and the associated emission.

- As found in planetary magnetospheres, such variations can excite MHD waves and even cascade to magnetic turbulence, leading to pitch-angle scattering of electrons (e.g. Summers et al. 2005; Kim et al. 2018) into a loss cone that allows interaction with the underlying planet or star. The

associated energy loss can compete with gyro-cooling, and so lower the overall radio emission.

- Both loss mechanisms lead to formation of anisotropic electron distribution. Future work should examine how this affects the associated electron cyclotron maser emission (ECME) seen from many such magnetic stars (e.g. Triguero et al. 2000; Das et al. 2022).

- Instead of the simplified assumption here of isotropic emission, future work should take into account the distinctive angular phase function for gyro-synchrotron emission.

- Within the CBO-driven reconnection paradigm, there is a need for detailed modeling, e.g. using particle-in-cell (PIC) codes (Lapenta 2012; Germaschewski et al. 2016), of the electron acceleration from reconnection, with a focus on the spatial deposition of non-thermal electrons.

- Does such reconnection yield non-gyrotropic electron deposition, and if so, does it favor field-aligned or orthogonal pitch angles? This is crucial for mirroring and the spatial distribution of radio emission.

- Finally, to test and constrain the basic gyro-cooling model and any extensions, there is a need for more extended observational programs on radio spectra and their level of variability on a dynamical timescale of order a day. While current radio observatories cannot spatially resolve the emission from hot-star magnetospheres, upcoming facilities such as the ngVLA (McKinnon et al. 2019) will have the sensitivity and angular resolution to do so for at least a subset of hot magnetic stars; this will allow direct tests of predictions from our simple model, and constrain characteristics of the underlying energy deposition processes.

Overall, despite the relatively idealized nature of its basic assumptions, the gyro-cooling analysis presented here forms a good initial basis for modelling the observed incoherent radio emission from these magnetic massive stars.

ACKNOWLEDGEMENTS

We thank the referee for their constructive comments that helped us to improve the manuscript significantly. BD acknowledges support from the Bartol Research Institute. The contributions by SPO are supported in part by the National Aeronautics and Space Administration under Grant No. 80NSSC22K0628 issued through the Astrophysics Theory Program.

DATA AVAILABILITY

This is a theoretical work, and does not use any observational data.

REFERENCES

- Andre P., Montmerle T., Feigelson E. D., Stine P. C., Klein K.-L., 1988, *ApJ*, 335, 940
 Aurière M., et al., 2007, *A&A*, 475, 1053
 Condon J. J., Ransom S. M., 2016, Essential Radio Astronomy. <https://www.cv.nrao.edu/~sransom/web/Ch5.html>
 Das B., Chandra P., 2021, *ApJ*, 921, 9

Das B., et al., 2022, *ApJ*, 925, 125
 Drake S. A., Abbott D. C., Bastian T. S., Biegging J. H., Churchwell E., Dulk G., Linsky J. L., 1987, *ApJ*, 322, 902
 Germaschewski K., Fox W., Abbott S., Ahmadi N., Maynard K., Wang L., Ruhl H., Bhattacharjee A., 2016, *Journal of Computational Physics*, 318, 305
 Grunhut J. H., et al., 2017, *MNRAS*, 465, 2432
 Güdel M., 2009, in Cargill P., Vlahos L., eds., Vol. 778, *Turbulence in Space Plasmas*. p. 269, doi:10.1007/978-3-642-00210-6_8
 Kim K.-H., Kim G.-J., Kwon H.-J., 2018, *Earth, Planets and Space*, 70, 174
 Kochukhov O., Shultz M., Neiner C., 2019, *A&A*, 621, A47
 Lapenta G., 2012, *Journal of Computational Physics*, 231, 795
 Leach J., Petrosian V., 1981, *ApJ*, 251, 781
 Leto P., Trigilio C., Buemi C. S., Umana G., Leone F., 2006, *A&A*, 458, 831
 Leto P., Trigilio C., Buemi C. S., Leone F., Umana G., 2012, *MNRAS*, 423, 1766
 Leto P., et al., 2021, *MNRAS*, 507, 1979
 McKinnon M., Beasley A., Murphy E., Selina R., Farnsworth R., Walter A., 2019, in *Bulletin of the American Astronomical Society*. p. 81
 Owocki S. P., Shultz M. E., ud-Doula A., Sundqvist J. O., Townsend R. H. D., Cranmer S. R., 2020, *MNRAS*, 499, 5366
 Owocki S. P., Shultz M. E., ud-Doula A., Chandra P., Das B., Leto P., 2022, *MNRAS*, 513, 1449
 Petit V., et al., 2013, *MNRAS*, 429, 398
 Shultz M., et al., 2019, *MNRAS*, 482, 3950
 Shultz M. E., et al., 2020, *MNRAS*, 499, 5379
 Shultz M. E., et al., 2022, *MNRAS*, 513, 1429
 Sikora J., Wade G. A., Power J., Neiner C., 2019, *MNRAS*, 483, 2300
 Summers D., Mace R. L., Hellberg M. A., 2005, *Journal of Plasma Physics*, 71, 237–250
 Trigilio C., Leto P., Leone F., Umana G., Buemi C., 2000, *A&A*, 362, 281
 Trigilio C., Leto P., Umana G., Leone F., Buemi C. S., 2004, *A&A*, 418, 593
 Virtanen P., et al., 2020, *Nature Methods*, 17, 261
 ud-Doula A., Owocki S. P., Townsend R. H. D., 2009, *MNRAS*, 392, 1022
 von der Linden J., Fiksel G., Peebles J., Edwards M. R., Willingale L., Link A., Mastro Simone D., Chen H., 2021, *Physics of Plasmas*, 28

APPENDIX A: RELATIVISTIC EQUATIONS

Let us now consider the generalization of the gyro-cooling equations for the relativistic case of electrons with an initial Lorentz factor $\gamma_a > 1$ at the loop apex, thus with associated energy is $E_a = (\gamma_a - 1)mc^2$.

The corresponding apex-scaled energy along the loop is thus now given by

$$e = \frac{E}{E_a} = \frac{\gamma - 1}{\gamma_a - 1},$$

so that

$$\gamma = 1 + (\gamma_a - 1)e. \quad (\text{A1})$$

The relativistic magnetic moment is given by (e.g. von der Linden et al. 2021):

$$P_m = \frac{\gamma m v^2 \sin^2 \alpha}{2B}.$$

Substituting $\sin^2 \alpha = pb/e$, $B = bB_a$, $v^2 = \beta^2 c^2 = c^2(\gamma^2 - 1)/\gamma^2$, we get

$$P_m = \left(\frac{\gamma + 1}{2\gamma} \right) \frac{pE_a}{B_a}. \quad (\text{A2})$$

Let us first consider the equation for the time evolution of $\mu = \cos \theta$. By setting $t \equiv t/t_a$, where $t_a = r_a/v_a$, we have

$$\frac{d\mu}{dt} = -\frac{\beta \cos \alpha}{\beta_a \sqrt{1 + 3\mu^2}},$$

which reduces to

$$\boxed{\frac{d\mu}{dt} = -\text{Sign}(\cos \alpha) \frac{\sqrt{e - pb}}{\sqrt{1 + 3\mu^2}} \left\{ \frac{\beta}{\beta_a \sqrt{e}} \right\}}, \quad (\text{A3})$$

where

$$\frac{\beta}{\beta_a \sqrt{e}} = \frac{\gamma_a \sqrt{2 + (\gamma_a - 1)e}}{(1 + (\gamma_a - 1)e)\sqrt{\gamma_a + 1}}. \quad (\text{A4})$$

Note that this relativistic correction factor reduces to unity when $\gamma_a \rightarrow 1$.

Let us next consider the relativistic form of the energy equation,

$$\frac{dE}{dt} = -\frac{\sigma_{\text{T}} c}{4\pi} \beta^2 \gamma^2 B^2 \sin^2 \alpha.$$

Again setting $t \rightarrow t/t_a$, $E = eE_a$, $B = bB_a$ and $\sin^2 \alpha = pb/e$, we find the relativistic generalization of the scaled energy equation (9 takes the form,

$$\boxed{\frac{de}{dt} = -k pb^3 \left\{ 1 + \frac{e(\gamma_a - 1)}{2} \right\}}, \quad (\text{A5})$$

where the cooling constant k is defined by eqn. (11).

Finally, we consider the equation for the time evolution of magnetic moment,

$$\frac{d}{dt}(\gamma m v \cos \alpha) = -\frac{P_m}{v \cos \alpha} \frac{dB}{dt}$$

Using eqns. A1, A2 and A5, we can cast this into the scaled form,

$$\boxed{\frac{dp}{dt} = \frac{1}{b} \frac{de}{dt} \left\{ 1 + \frac{(e - pb)(\gamma_a - 1)}{(\gamma_a - 1)e + 2} \right\}}. \quad (\text{A6})$$

Eqns. (A3), (A5) and (A6) represent the relativistic generalizations of the non-relativistic forms (14), (9), and (10). In each case the relativistic correction factor, enclosed in curly brackets, reduces to unity in the non-relativistic limit $\gamma_a \rightarrow 1$.